Cwc27, associated with retinal degeneration, functions as a splicing factor *in vivo*

Renae Elaine Bertrand[1,2], Jun Wang[2,3], Yumei Li[2,3], Xuesen Cheng[2], Keqing Wang[2,3], Peter Stoilov[4] and Rui Chen [2,3,*]

[1]Department of Biochemistry and Molecular Biology, Baylor College of Medicine, Houston, TX 77030, USA
[2]Human Genome Sequencing Center, Baylor College of Medicine, Houston, TX 77030, USA
[3]Department of Molecular and Human Genetics, Baylor College of Medicine, Houston, TX 77030, USA
[4]Department of Biochemistry, West Virginia University, Morgantown, WV 26506, USA

*To whom correspondence should be addressed at: Department of Molecular and Human Genetics, Baylor College of Medicine, One Baylor Plaza, Houston, TX 77030, USA. Tel: +1 7137985194; Fax: 7137985741; Email: ruichen@bcm.edu

Abstract

Previous *in vitro* studies indicate that CWC27 functions as a splicing factor in the B^{act} spliceosome complex, interacting with CWC22 to form a landing platform for eIF4A3, a core component of the exon junction complex. However, the function of CWC27 as a splicing factor has not been validated in any *in vivo* systems. CWC27 variants have been shown to cause autosomal recessive retinal degeneration, in both syndromic and non-syndromic forms. The *Cwc27$^{K338fs/K338fs}$* mouse model was shown to have significant retinal dysfunction and degeneration by 6 months of age. In this report, we have taken advantage of the *Cwc27$^{K338fs/K338fs}$* mouse model to show that Cwc27 is involved in splicing *in vivo* in the context of the retina. Bulk RNA and single cell RNA-sequencing of the mouse retina showed that there were gene expression and splicing pattern changes, including alternative splice site usage and intron retention. Positive staining for CHOP suggests that ER stress may be activated in response to the splicing pattern changes and is a likely contributor to the disease mechanism. Our results provide the first evidence that CWC27 functions as a splicing factor in an *in vivo* context. The splicing defects and gene expression changes observed in the *Cwc27$^{K338fs/K338fs}$* mouse retina provide insight to the potential disease mechanisms, paving the way for targeted therapeutic development.

Introduction

Splicing of pre-mRNA is the process of removing non-coding, intronic regions and joining together exons to form messenger RNA (mRNA) which can be translated to functional proteins, and it is catalyzed by a large complex known as the spliceosome. The spliceosome is composed of small nuclear ribonucleoproteins and various other splicing factors and is capable of performing such a precise process through a controlled stepwise assembly and conformational and compositional changes of the spliceosome itself (1). Through the splicing process, multiple mRNA isoforms can be generated, known as alternative splicing of transcripts, to tune the expression levels of mRNA isoforms (2), their temporal expression (3) and tissue specificity (4). Disruption of the careful process of splicing can result in mis-splicing of RNA transcripts, causing events such as intron retention, aberrant alternative splice site usage and exon skipping. Mutations in spliceosome components invariably result in aberrant splicing and are associated with diseases such as cancer (5,6), craniofacial defects (7–9) and neurodegeneration (10–14). Transcriptome analyses in genetic models of both retinal degeneration (RD) and spinal muscular atrophy (SMA) where core splicing factors are affected show evidence of perturbed splicing, including increased intron retention and aberrant

alternative splicing (12,15). In a mouse model of SMA, RNA-sequencing revealed some differential gene expression (DGE), and an increase in intron retention and alternative splicing, suggesting that aberrant splicing is driving the SMA pathology (16).

Autosomal dominant retinitis pigmentosa is a form of RD known to be associated with mutations in the splicing factor genes *PRPF31* (17), *PRPF8* (14), *PRPF6* (13), *PRPF4* (11) and *SNRNP200* (18). Despite the ubiquitous expression of these splicing factors, mutations do not result in syndromic forms of disease, but rather they explicitly cause autosomal dominant retinitis pigmentosa with no other reported clinical diagnoses. One key limitation to further studying the mechanisms behind splicing factor associated RD is the difficulty in establishing murine models that exhibit phenotypes consistent with the human phenotype, making it impossible to do detailed studies *in vivo*. Several mouse models of patient mutations in *Prpf3*, *Prpf8* and *Prpf31* were evaluated for retinal disease but failed to recapitulate patients' phenotypes (19). Nevertheless, the knockout models and other *Prpf31* knock-in mouse models did show retinal pigmented epithelium (RPE) degenerative phenotypes in the heterozygous state, including accumulation of amorphous deposits between the RPE and Bruch's membrane and phagocytosis deficiency (19–21). Although the

mouse models did not recapitulate patient phenotypes, they still provided some insight to how splicing factor mutations impact the transcriptomes of retinal cells *in vivo*. RNA-sequencing of the *Prpf31* models (21,22) and RP11 (*PRPF31*-caused RP) patient-derived retinal organoids and RPE (10) showed splicing pattern changes, including increased intron retention and alternative 3′ splice site usage. Splicing pattern changes, consistent with those caused by *PRPF31* mutations, are observed with loss of *prpf8* in zebrafish and knocked down *PRPF8* in Cal51 cells, including increases in both intron retention and alternative exon usage (23,24). There is a consensus that altered splicing profiles are causative of the disease phenotypes, though the exact splicing changes and genes affected differ between models. Despite these advancements in the understanding of how splicing factor mutations result in RD, there still exists the gap of studying how the transcriptome is affected in an *in vivo* model of RD which accurately recapitulates the patient phenotype.

CWC27 (NM_005869) is a gene associated with both syndromic and non-syndromic forms of RD with a recessive inheritance pattern (25,26). In addition to RD, patients with severe mutations in *CWC27* exhibited a range of clinical phenotypes such as brachydactyly and neurological defects. The *CWC27* protein consists of a N-terminal cyclophilin peptidyl-prolyl *cis-trans* isomerase (PPIase) domain and unstructured C-terminus (27,28). The PPIase domain of the CWC27 lacks *cis-trans* isomerase activity but is still capable of binding proline and is believed to be involved in protein–protein interactions (29). The elongated, solvent-exposed C-terminal end (29) of CWC27 interacts with CWC22 to form a landing platform to recruit eIF4A3, the core component of the exon junction complex (EJC), to the spliceosome (28,30). *In vitro* studies show that CWC27 associates with the spliceosome and participates in the B^{act} complex and is released from the spliceosome prior to conversion to the B* complex and assembly of the complete EJC (27,31). Despite all evidence that suggests that CWC27 functions as a splicing factor, this function has not been previously tested *in vivo*. Previous attempts to determine its functional significance in yeast models failed to associate a phenotype with its loss or show function in splicing (32–34). A *Cwc27* knockout mouse proved to be largely embryonic lethal in the homozygous state but showed no retinal phenotype in the heterozygous state (26), consistent with other splicing factor knockout mouse models. Interestingly, a knock-in mouse model, *Cwc27*$^{K338fs/K338fs}$, was not embryonic lethal and exhibited a 50% reduction in retinal function by electroretinography and a 50% decrease in retinal thickness by morphological studies (26). In RPE1 cells, knockdown of *CWC27* resulted in increased intron retention and it was hypothesized that inflammation may be a driver of the RD observed in patients (28). In this study, the progression of RD in the *Cwc27*$^{K338fs/K338fs}$

mouse model is characterized, the retinal transcriptome is evaluated to determine if Cwc27 contributes to splicing of pre-mRNA transcripts *in vivo* and we identify several mechanisms that likely contribute to the observed degeneration phenotype.

Results
Mutant mice exhibit progressive RD

To characterize the progression of RD in the *Cwc27* mutant mice, electroretinography (ERG) and histological analysis was performed at multiple time points. At 2 months of age, ERGs for the homozygous mutant mice show no significant difference across all flash strengths for both scotopic and photopic waves compared with age matched controls (Fig. 1A). In contrast, by 3 months of age, the homozygous mutant mice show significantly lower responses at the highest flash strengths for both scotopic and photopic b-waves, with an average 26% reduction in the scotopic b-wave and 33% reduction in the photopic b-wave (Fig. 1A). While the 3-month homozygous mutants do not show statistically significant decreases in the scotopic a-wave compared with controls, there is a decreasing trend across the highest flash strengths (Fig. 1A). Since the b-wave showed significant decreases at 3 months of age and this is normally attributed to inner retinal dysfunction and degeneration, we used PKC-a to identify if the ON-bipolar cell population, the major contributor to the b-wave, showed any significant degeneration and we did not observe any obvious differences in the mutant retina compared with the control (Supplementary Material, Fig. S1).

To check if the onset of RD coincides with functional defects, the number of rows of photoreceptor nuclei was counted at regularly spaced intervals across the outer nuclei layer (ONL) for both homozygous mutants and controls at various time points. Interestingly, there is no statistically significant degeneration observed across the retina in homozygous mutant mice compared with controls at 3 months of age (Fig. 1B and C), but by 4 months of age, the number of nuclei in the ONL is reduced by ~15% when comparing homozygous mutant mice to controls (Fig. 1B and C). Therefore, it appears that the functional decline slightly precedes photoreceptor degeneration.

The gene expression profile is altered in the mutant retina

Previously, CWC27 has been predicted to function as a splicing factor based on *in vitro* studies but its function as a splicing factor *in vivo* has not been reported. Leveraging the *Cwc27*$^{K338fs/K338fs}$ mouse model, RNA sequencing experiments were performed to determine if aberrant mRNA expression or splicing is observed in the mutant mouse retina compared with controls. To evaluate the gene expression profile at an early
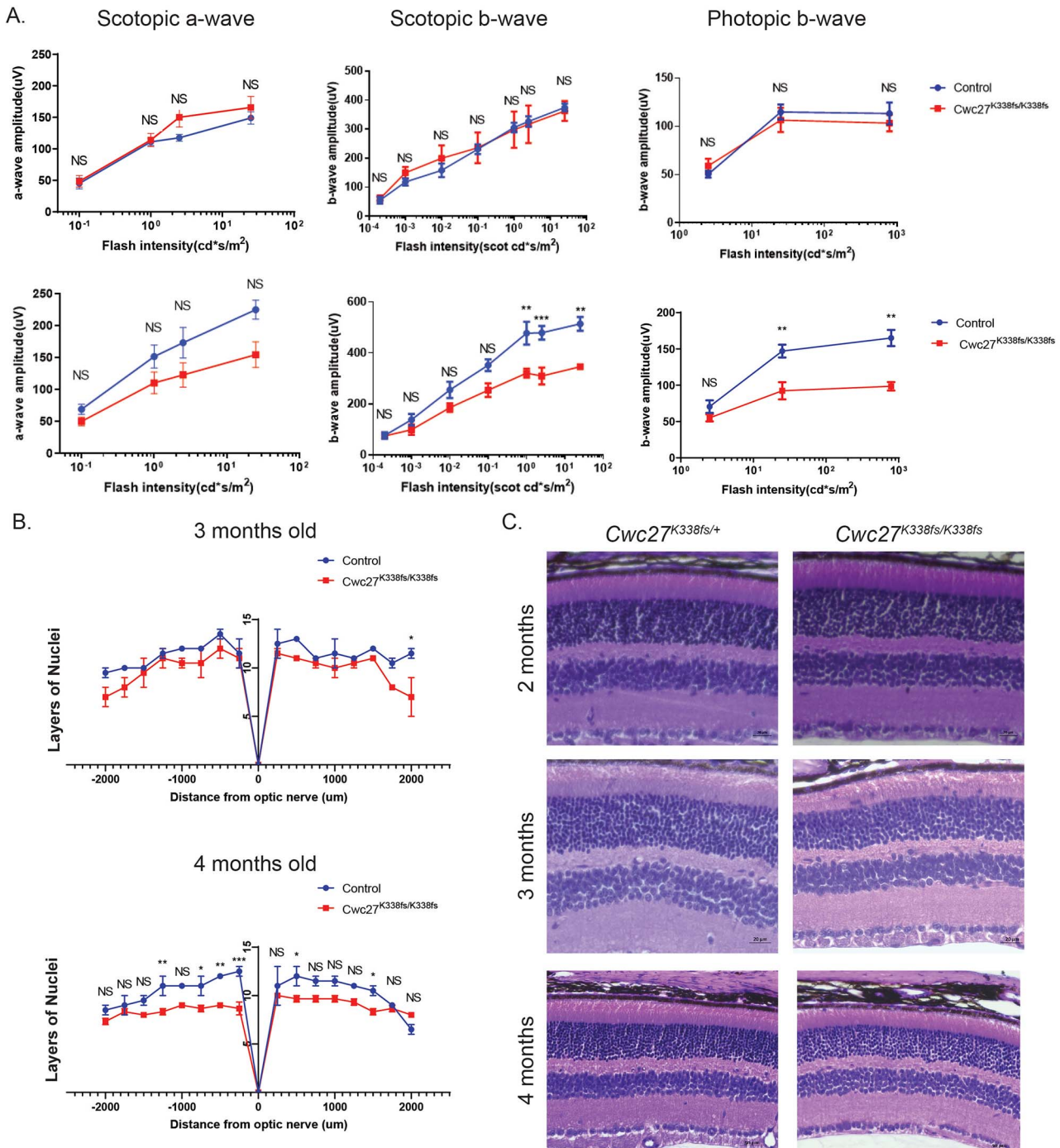
Figure 1. *Cwc27*$^{K338fs/K338fs}$ mice exhibit progressive RD. (**A**) Electroretinography was used to measure retinal dysfunction in mutant and control retinas. At 2 months of age (top), there is no observed significant differences in scotopic or photopic ERG waves between mutant ($n=3$) and control ($n=5$) mice. At 3 months of age (bottom), the mutant mice ($n=5$) show significantly reduced responses at the highest flash intensities for both scotopic and photopic b-waves compared with controls ($n=8$). (**B**) The number of nuclei layers in the ONL was counted for control ($n=3$) and mutant ($n=3$) mice for multiple time points. At 3 months of age, there is not a significant difference in the nuclei number between controls and mutant mice. At 4 months of age, there is significant loss of photoreceptors in the ONL. (**C**) Representative H&E brightfield images for 2-, 3- and 4-month-old heterozygous and homozygous mutant mice. Each dot represents the mean ± SEM. * = P-value ≤ 0.05, ** = P-value ≤ 0.01, *** = P-value ≤ 0.001, NS = not significant.

timepoint without the potential complication of cell death, mRNA-sequencing (RNA-seq) was performed for retinal tissue samples collected from three mutant mice and six wildtype mice at 3 months of age where there is no significant cell degeneration detected. High-quality RNA-seq was obtained with near perfect correlation of expression levels for the majority of genes observed among the nine samples (Supplementary Material, Fig. S2) (pair-wise Pearson correlation coefficients of the transformed gene expression are about 1 with P-value < 0.001 across the nine samples). To investigate which genes are expressed differently between mutant and wildtype control retinas, DEG analysis was performed. Consistent with the observation that all nine samples
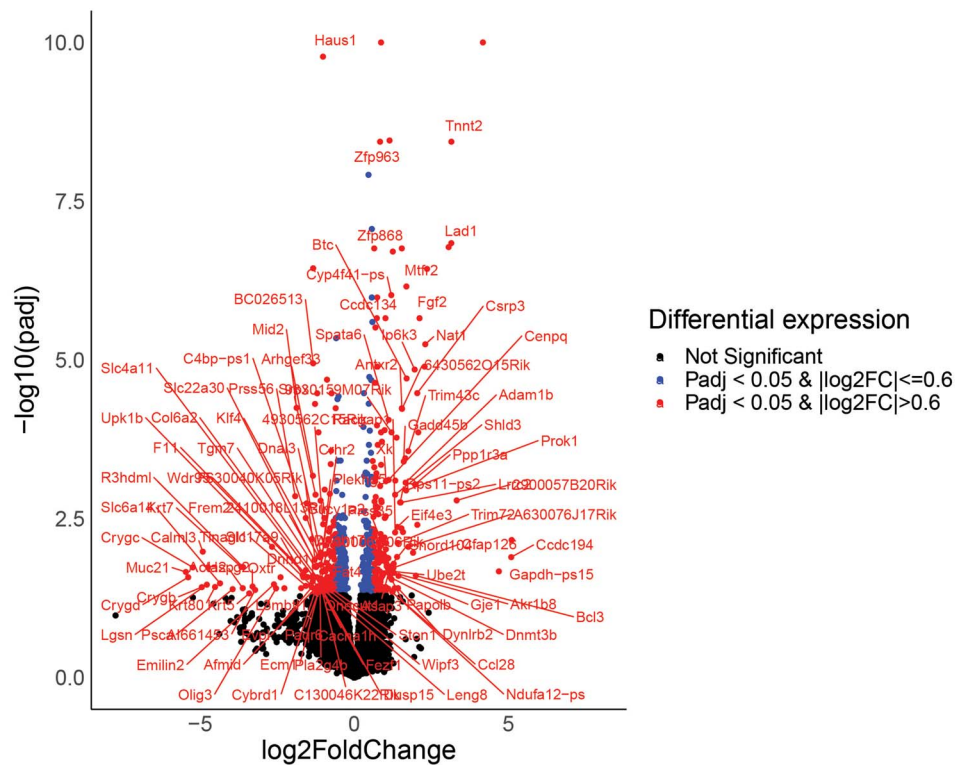
Figure 2. There are few gene expression changes observed from bulk RNA-seq in the mutant retina. The volcano plot shows DGE from the bulk RNA-seq between the homozygous mutant ($n = 3$) and wildtype control mice ($n = 6$). The genes with P_adj < 0.05 and |log2FC| ≤ 0.6 are labeled with blue. The genes with P_adj < 0.05 and |log2FC| > 0.6 are labeled in red. All genes with P_adj < 0.05 and |log2FC| ≥ 1 are labeled with their gene name. Genes with P_adj ≤ 10^{-10} were assigned as P_adj = 10^{-10} to improve the readability of the graphs.

exhibit very similar expression patterns, only a small number of DEGs are identified, including 165 up-regulated and 177 down-regulated genes (DEG analysis was performed with DESeq2, adjusted *P*-value < 0.05, |log2FC| > 0.6; FC: Fold change) (Fig. 2, Supplementary Material, Table S1), respectively. Gene ontology (GO) term analysis was performed on the DEGs (with P_adj < 0.05 and |log2FC| > 0.6; see Methods section for details) to determine if up- or down-regulated genes in the mutant retina converged on any specific pathways and they did not show any significant enrichment.

Since the bulk RNA-seq gives the average expression change, it is possible that DEGs restricted to rare cell types are not observed by bulk RNA-seq; therefore, single cell RNA sequencing (scRNA-seq) was utilized to determine if there are cell-type-dependent roles for Cwc27 or cell-type-specific pathology by transcriptome analysis of the homozygous mutant mouse retina. Since the 3-month mutant mouse retina shows relatively few changes in gene expression, we decided to examine the 4-month time point by scRNA-seq, when we would expect more significant transcriptome changes to occur with relatively minimal secondary effects since the degeneration has just begun, with ~85% of photoreceptor cells remaining. Retinal cups were isolated from mutant ($n = 1$) and wildtype ($n = 1$) mice and scRNA-seq was performed using the 10× Genomics platform. After data quality control (see Methods section), we performed

cluster analysis on the scRNA-seq data and identified the major known cell types in the retina in both the mutant and wildtype samples (Fig. 3A, Supplementary Material, Fig. S3). Consistent with previous reports, in the wildtype control retina, rod photoreceptors are the most abundant cell type at 74% (Table 1). Then, we sought to evaluate the DEGs in each cell type between the mutant and wildtype retinas. We first aligned cell clusters from these two samples, and as shown in Fig. 3B, all cell types could be readily matched. We found that two major cell types, rod photoreceptors and Muller glial (MG) cells, have the largest number of DEGs observed with 67 (54 up-regulated genes and 13 down-regulated genes in rod photoreceptors; Fig. 4A, Supplementary Material, Table S2) and 39 (37 up-regulated genes and 2 down-regulated genes in MG cells; Fig. 4B, Supplementary Material, Table S3) DEGs, respectively (scRNA DEG analysis was performed with Wilcoxon rank sum test via Seurat; Adjusted *P*-value < 0.05, log2FC > 0.6, or < −0.6, see Methods section). To determine if the DEGs have enrichment in any interesting pathways, GO term analysis was performed on the DEGs (the DEGs with adjusted *P*-value < 0.05, log2FC > 0.6, or < −0.6). For rod photoreceptors, GO term analysis (35–37) reveals that the down-regulated genes are enriched for mitochondrial encoded transcripts (Fig. 4C, Supplementary Material, Fig. S4A); this finding is consistent with the results from a previous study where

Table 1. The number of cells assigned to each cell-type cluster from the scRNA-seq performed on 4-month-old mutant and wildtype mouse retinas

| Cell type	$Cwc27^{K338fs/K338fs}$		Wildtype	
	No. of cells	Propor-tion	No. of cells	Propor-tion
Amacrine cells	69	0.6%	95	1.0%
Bipolar cells	955	8.7%	994	10.5%
Cone photoreceptors	384	3.5%	511	5.4%
MG cells	703	6.4%	766	8.1%
Retinal ganglion cells	85	0.8%	120	1.3%
Rod photoreceptors	8732	79.9%	6987	73.8%
Total	10 928	100%	9473	100%

they knocked down CWC27 in RPE1 cells and found down regulation of mitochondrial encoded transcripts related to oxidative phosphorylation enzymes (28). There are no significantly enriched terms for up-regulated genes in the rod photoreceptors. In MG cells, GO term analysis (35–37) identified the upregulation of genes related to inflammation (Fig. 4D, Supplementary Material, Fig. S4B, Supplementary Material, Table S3) which is consistent with both MG cell activation, which has previously been reported to be induced by photoreceptor degeneration (38,39), and again the CWC27 knockdown study in RPE1 cells, which found upregulation of pro-inflammatory genes (28). Cone photoreceptors, which show dysfunction by photopic ERGs (Fig. 1A) and constitute a small propor-tion of the cells evaluated by scRNA-seq (Table 1), had only a small number of significant DEGs identified, with three up-regulated and one down-regulated genes (Sup-plementary Material, Fig. S5A, Supplementary Material, Table S4). The other retinal cell types, including bipolar cells (Supplementary Material, Fig. S5B, Supplementary Material, Table S5), retinal ganglion cells and amacrine cells, did not show evidence of a significant phenotype in the mutant mouse and showed minimal gene expression changes (Supplementary Material, Tables S5–S7). When comparing the gene expression changes between *Cwc27* mutant and wildtype of bulk RNA-seq in the 3-month-old mice with those of the scRNA-seq in the 4-month-old mice, the gene expression changes of bulk retina showed the most significant correlation with those of rods (Pearson correlation, $R = 0.41$, P-value $< 2.2 \times 10^{-16}$, Supplementary Material, Fig. S5C) and a less significant correlation with MG cells (Pearson correlation, $R = 0.1$, P-value $< 2.2 \times 10^{-16}$, Supplementary Material, Fig. S5D) but no significant correlation with cones or bipolar cells.

Splicing analysis identifies increased splicing changes in the mutant retinal cells

RNA sequencing of tissues from various models of splicing factor mutations revealed changes to splicing patterns, although the types of changes and genes affected differed between models, the general molecular phenotype was consistent. Based on *in vitro* functional studies in conjunction with the RNA-seq results from previous splicing factor-associated disease models, we anticipate that the splicing profile in the $Cwc27^{K338fs/K338fs}$ mouse retina will also be altered if *Cwc27* is functioning as a splicing factor *in vivo*. In the 3-month-old mouse bulk RNA-seq data, the comparison of the splicing profile between $Cwc27^{K338fs/K338fs}$ and wildtype mouse retinas [measured by difference of the percent spliced in (PSI) value] was used to identify differential splicing events associated with the *Cwc27* mutation in the retina. We identified 257 differential splicing events in the mutant retina compared with wildtype (see Methods section for analysis details). The most abundant splicing changes observed in the mutant retina are intron retention followed by exon skipping (Fig. 5A), which are consistent with the types of splicing pattern changes observed in models such as the RP11 retinal organoids (10). We leveraged GO term enrichment analysis to determine if the genes identified to have splicing changes converged on any pathways. When using the molecular signatures database, GO term enrichment analysis of differentially spliced genes showed enrichment in visual electrophys-iology, including *Cnga1*, *Rpgrip1* and *Prpf6*, and protein demethylase associated genes, such as *Kdm2a* and *Kdm5b* (Fig. 5B), Supplementary Material, Fig. S6A. Consistent with these findings, disease ontology semantic and enrichment analysis (40) shows an enrichment in retinal disease associated genes among the differentially spliced genes (Supplementary Material, Fig. S6B and C). These results indicate that the mutation in *Cwc27* leads to increased intron retention, increased exon skipping and differential splice site usage in the retina.

The alternative splicing events were classified into three groups: alterations to coding exons, alterations in untranslated regions (UTRs) and alterations in non-coding regions. The splicing changes themselves were assigned as either intron retention, cassette exon (exon skipping or exon inclusion), alternative 5′ splice site or alternative 3′ splice site. Most splicing alterations detected in the mutant retina affect coding exons, while alterations in non-coding regions and UTRs are the least abundant (Fig. 5C) and retained introns were the most abundant type of alternative splicing event observed (Fig. 5C). In wildtype mice, the gene expression level (average TPM across wildtype samples) of the genes showing differential splicing ($n = 218$) was significantly higher than that of all tested genes ($n = 9021$) (Wilcoxon rank sum test, one tailed, P-value $= 0.001034$) (Fig. 6A), suggesting that the splicing of highly expressed genes is more likely to be affected when *Cwc27* is mutated. Interestingly, significantly increased intron retention and exon skipping were detected in several inherited retinal disease genes, including *Cnga1*, *Prpf6 and Rpgrip1* (Fig. 6B–D, Supplementary Material, Table S8), in the retinas of homozygous mutant mice compared with controls. The identified intron retention events and the
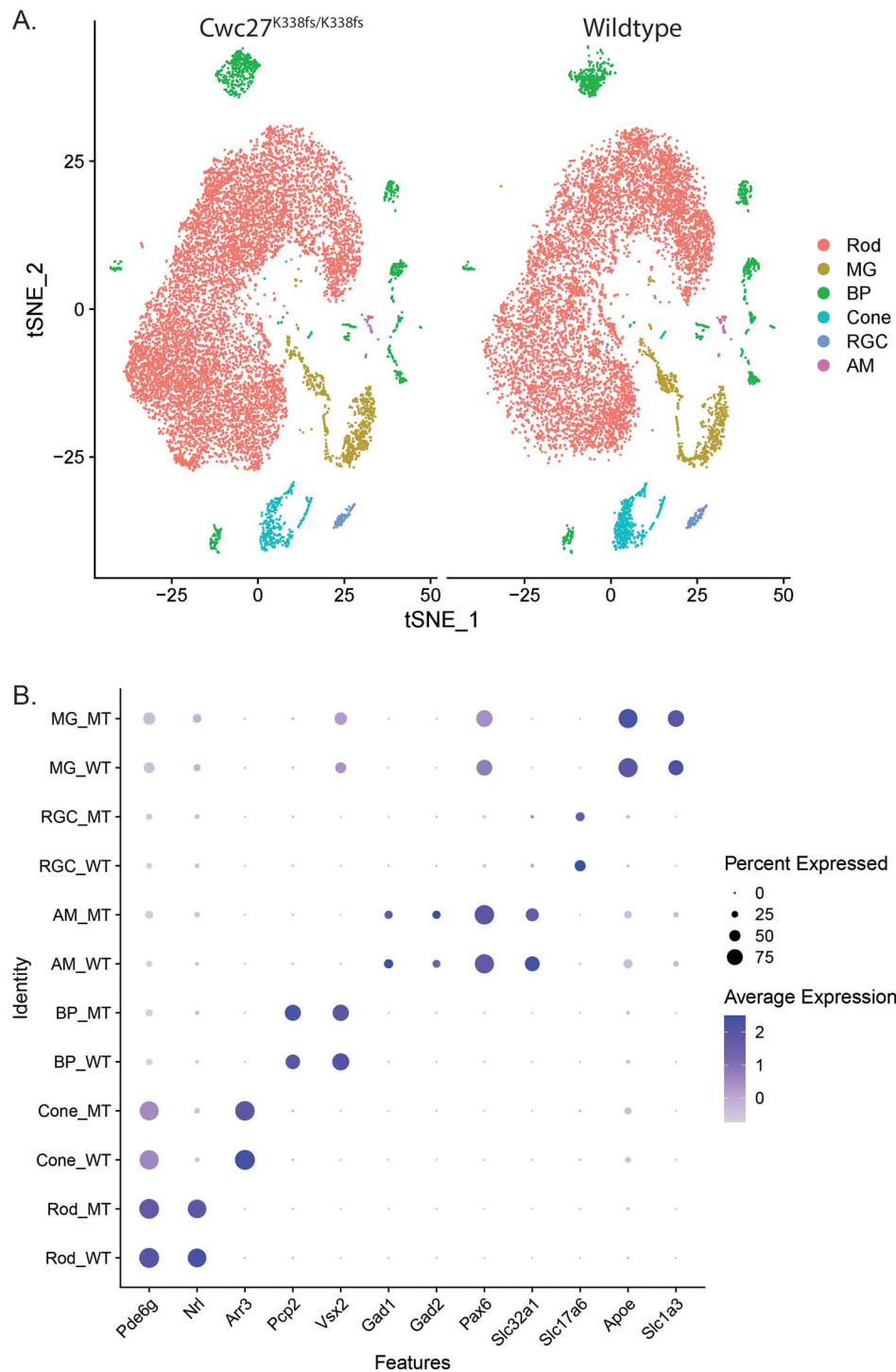
Figure 3. The single cell RNA-seq data are high quality and all cell-types can be identified in the mutant and wildtype samples. (**A**) Cell type clustering for the homozygous mutant retina (*n* = 1) and wildtype control (*n* = 1) using 10 × 3′ single cell RNA sequencing data. (**B**) Quality control of the 10× scRNA-seq cell clustering by cell-type marker expression. AM = amacrine cells; BP = bipolar cells; Cone = cone photoreceptors; MG = Muller glial cells; RGC = retinal ganglion cells; Rod = rod photoreceptors.

related statistics are listed in Supplementary Material, Table S8.

Cnga1, a cyclic nucleotide-gated channel important for phototransduction in photoreceptors, has been shown to cause RD with an autosomal recessive inheritance pattern (41) and is one of the top results for increased intron retention with ∼29% of the transcripts determined to have the retained intron (Fig. 6B, Supplementary Material, Table S8). To validate the intron retention observed in *Cnga1* transcripts, reverse-transcription PCR (RT-PCR) was performed using RNA extracted from mutant and control retinas. The PCR design included
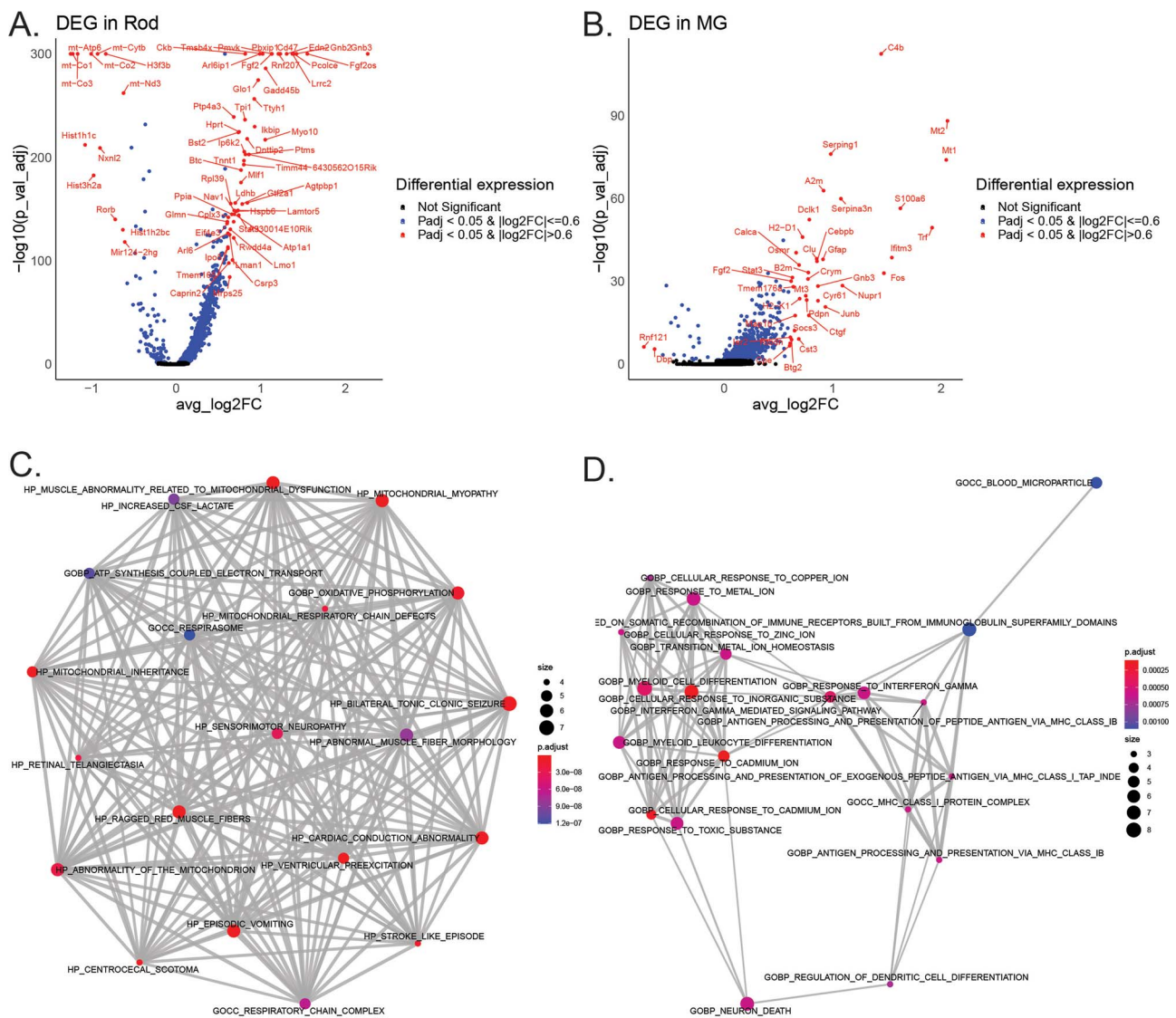
Figure 4. Rods and MG cells have the most gene expression changes observed. (**A**) Volcano plot depicting the DGE between mutant and wildtype rod photoreceptors. There are 67 DEGs in rod photoreceptors. The genes with $P\_adj < 0.05$ and $|\log_2 FC| \leq 0.6$ are labeled with blue. The genes with $P\_adj < 0.05$ and $|\log_2 FC| > 0.6$ are labeled with red. The genes with $P\_adj < 0.05$ and $|\log_2 FC| > 0.6$ were labeled with their gene name. The genes with $P\_adj \leq 10^{-300}$ were assigned as $P\_adj = 10^{-300}$. (**B**) Volcano plot depicting the DGE between mutant and wildtype MG cells. There are 39 DEGs. The genes with $P\_adj < 0.05$ and $|\log_2 FC| \leq 0.6$ are labeled with blue. The genes with $P\_adj < 0.05$ and $|\log_2 FC| > 0.6$ are labeled with red. The genes with $P\_adj < 0.05$ and $|\log_2 FC| > 0.6$ were labeled with their gene name. (**C**) The network shows the relationship of the down-regulated genes within biological pathways identified by GO term analysis in rods photoreceptors. There is enrichment of mitochondrial related genes. (**D**)The network shows the relationship of the up-regulated genes within the biological pathways identified by GO term analysis in MG cells. There is enrichment of genes related to the inflammatory response and other stress-related pathways. The color scale shows the adjusted *P*-value for GO enrichment. The dot size shows the number of genes in each GO term. For all volcano plots, if the gene is a gene model (name follows format Gm[0–9]*), the gene name was not labeled on the plot even if they fit the criteria to be included to reduce the density of text in the plots.

primers in the exons flanking exon 5, which gives a longer product when intron 5 is retained and is only observed in the mutant retina (Fig. 6E). To evaluate if the intron retention detected in the *Cnga1* gene transcripts results in changes to the protein expression, immunofluorescent staining for Cnga1 was performed in mutant and control retinal cross-sections. Immunofluorescent staining for Cnga1 shows reduced protein expression but the correct protein localization to the outer segments of photoreceptors in the mutant mouse retina (Fig. 6F).

The intron retention detected in RNA transcripts in the mutant retina can result in truncated proteins following translation with or without NMD activation. To determine if ER stress is activated in the photoreceptors of homozygous mutant mice, immunofluorescent staining for CHOP was conducted. CHOP (DDIT3) is normally expressed at low levels but is induced under chronic ER stress conditions, leading to the initiation of apoptosis to clear damaged cells. Immunofluorescent staining in 2-month-old mutant and control retinal cross-sections did not show any significant detectable
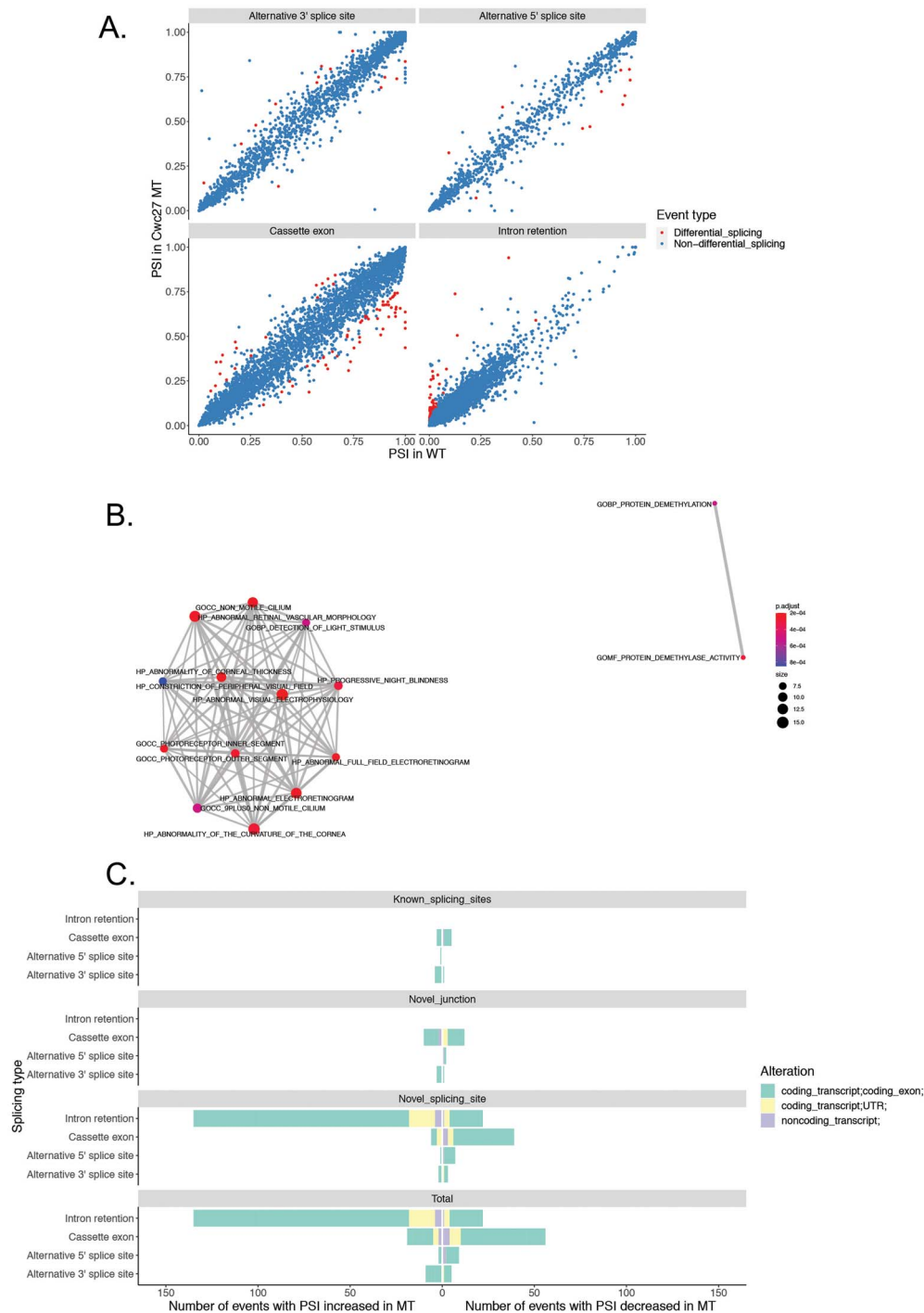
Figure 5. Increased intron retention is observed in the *Cwc27^{K338fs/K338fs}* mouse retina. (**A**) A plot of the average PSI ratios between mutant and wildtype bulk retina RNA-seq for each of four types of splicing alterations; 257 differential splicing events (red) were observed across all types of splicing alterations. (**B**) The networks show the relationship of the differentially spliced genes within biological pathways identified by GO term analysis and revealed that there was enrichment in genes associated with visual electrophysiology. (**C**) Splicing events plotted by splicing type and region of the alteration (affecting coding exons, UTR or non-coding region). The splicing alterations were further categorized as using known splice sites, a novel junction or novel splice sites. The most significant splicing changes were increased intron retention (introns with increased PSI in mutant; 135 events) and increased exon skipping (exons with decreased PSI in the mutant; 56 events).

CHOP expression in either sample (Fig. 6G). Since the onset of degeneration does not occur until 4-months-old, immunofluorescent staining for CHOP was repeated in retinal cross sections from mice at 4 months old. At 4 months of age, immunofluorescent staining detected induction of CHOP in photoreceptors of mutant mice but is not detected in age matched controls (Fig. 6G).

Discussion

Many RD patients have disease caused by mutations in core spliceosome components but, despite a concerted effort to model these mutations in mice, the *Cwc27*^{K338fs} mice are the first mouse model of a core spliceosome component that recapitulates the human phenotype and also clearly shows a splicing defect. Importantly, CWC27 has been shown to associate with the B^{act} spliceosome complex and have proline binding activity all by *in vitro* experimentation (27,28); however, yeast studies failed to demonstrate a requirement for CWC27 in splicing (27,28,32–34). It was previously shown that knockdown of CWC27 by siRNA in hTERT-RPE-1 cells causes increased intron retention and a wide impact on gene expression, including up-regulation of pro-inflammatory genes and down-regulation of genes associated with the transforming growth factor beta signaling cascade, actin cytoskeleton and mitochondrial genes (28). Here, we used the *Cwc27*^{K338fs/K338fs} mouse, which shows onset of photoreceptor dysfunction at 3 months of age and onset of photoreceptor cell degeneration at 4 months of age, to test the function of Cwc27 *in vivo* for the first time. Consistent with the findings from RPE1 cells upon knockdown of CWC27, we observed changes to both the splicing profile and gene expression profile in the *Cwc27*^{K338fs/K338fs} mouse retina. Splicing analysis of the RNA-sequencing data from 3-month-old *Cwc27*^{K338fs/K338fs} and control mouse retinas revealed significantly increased intron retention, alternative exon usage and alternative splice site usage. These changes are dependent on the *Cwc27* genotype, indicating that Cwc27 plays a direct role in the splicing of the affected genes which supports the hypothesis that CWC27 is a splicing factor. This is the first direct evidence that Cwc27 functions in a splicing factor capacity *in vivo*.

As expected, based on findings from both *CWC27* and other splicing factor mutation models, gene expression was also impacted in the *Cwc27*^{K338fs/K338fs} retina. We first evaluated DGE at 3 months of age; however, few DEGs were identified. Based on the phenotypic data presented here, we hypothesized that the 4-month-old mice may have more significant gene expression changes as this is the onset of photoreceptor degeneration. We performed 10× single cell RNA-sequencing on the retinas of 4-month-old *Cwc27*^{K338fs/K338fs} and control mice. DEG analysis of the 4-month-old mouse retinas revealed similar trends of gene expression changes between *Cwc27* mutant and wildtype compared with the bulk retina RNA-sequencing at 3 months of age. The largest numbers of DEGs were identified in rods and MG cells, with more up-regulated genes than down-regulated genes in the mutant retina. Although the ERGs show that the b-wave, derived from the inner retinal cell function, is more significantly decreased than the a-wave, which is derived from photoreceptor function, we did not see any significant degeneration of bipolar cells which are the major contributors to the b-wave. It is possible that

the bipolar cells are also affected; however, we did not identify large numbers of significant DEGs specific to bipolar cells or other inner retinal cell types and we were not able to perform the splicing analysis on a single cell level so a deeper study of the molecular consequences of the mutant Cwc27 on bipolar cells and the other inner retinal cells was not performed here. The upregulation of inflammatory response genes in MG cells is consistent with the findings from the knockdown of *CWC27* in RPE1 cells, but there are some significant differences between the two data sets in regard to splicing changes which are likely due to a combination of differences in cell-type and severity of the impact on the CWC27 protein.

The molecular consequences of the *Cwc27*^{K338fs} allele include changes to both the splicing and, to a lesser extent, the gene expression profiles. The increased intron retention in the *Cwc27*^{K338fs/K338fs} mouse retina can have a dramatic effect on the retinal cells. We detected 152 genes to be affected by intron retention and we expect this to be an underestimation since a significant number of transcripts with retained introns should be degraded by nonsense mediated decay. Intron retention has been shown to cause cell death via the innate immune response in cancer cells that are sensitive to splicing stress and it is possible that the retinal cells are also in this stressed state and sensitive to splicing changes (42). One important piece of evidence that suggests that the eye is particularly sensitive to splicing changes is the finding that when cancer patients were treated with splicing inhibitors, several experienced vision loss to due to optic nerve damage, suggesting that the eye in particular is sensitive to splicing changes (43,44). Beyond the direct cause and effect of intron retention, in the *Cwc27*^{K338fs/K338fs} retina, we observed activation of ER stress by increased levels of CHOP by immunofluorescent staining. This could be activated by transcripts with retained introns being translated into truncated or misfolded proteins. It has been well recorded that the activation of ER stress can lead to photoreceptor degeneration, and together with our observation in the *Cwc27*^{K338fs/K338fs} retina, this suggests that intron retention and the secondary ER stress are likely contributing to the RD phenotype, though to what extent is still unclear. It is very possible that the other differential splicing events and DEGs contribute to the phenotype as well, but it is unclear to what degree each is driving the mutant phenotype. To further study the role of intron retention on the phenotype, we plan to use retinal explants treated with NMD inhibitors to determine how many genes and transcripts are truly affected by the *Cwc27*^{K338fs} allele and how this mechanism may be driving the phenotype.

Based on our observations in the *Cwc27*^{K338fs/K338fs} mouse, we hypothesize that in *CWC27* patients, the differential splicing is driving the disease, while the DGE is secondary. Based on our current results, the FCs of the differentially expressed genes are not very large changes. It seems more likely that the differential splicing is
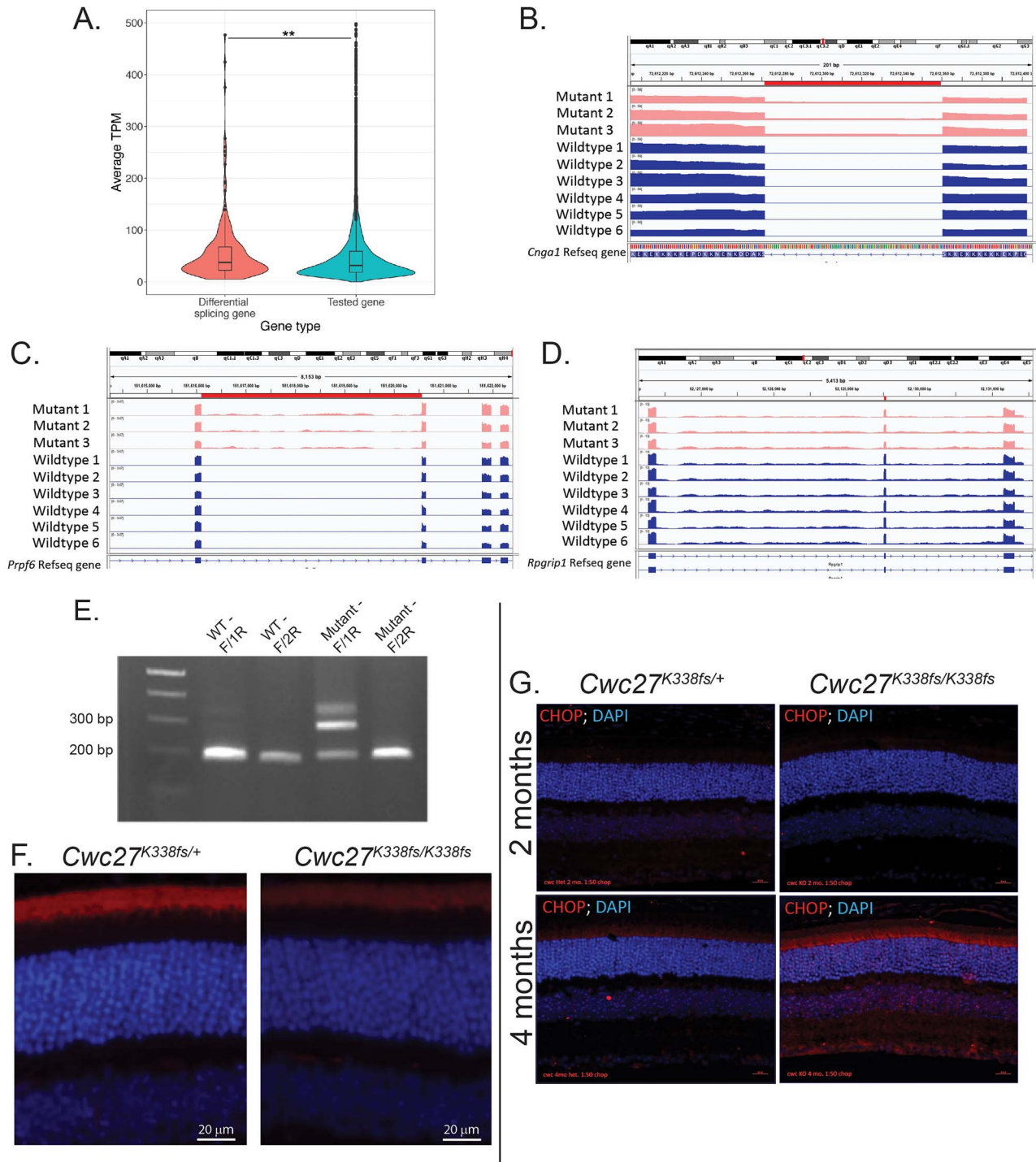
Figure 6. Intron retention has downstream consequences. (**A**) The gene expression level (average TPM) in WT mice of the genes showing differential splicing ($n = 218$) was significantly higher than that of all tested genes ($n = 9021$) (Wilcoxon rank sum test, one tailed, P-value = 0.001034). The violin plot showed gene expression level of the two groups of genes with the average TPM across the wildtype samples ≤ 500. (**B**) Bulk retinal RNA-seq reads mapped to the mouse reference genome (mm10) in the *Cnga1* gene show increased reads to the intronic region in the mutant mouse retinas compared with wildtype. Differential PSI = 0.2884. (**C**) Intron retention is observed in *Prpf6* transcripts from bulk retina RNA-seq. Reads were mapped to the mouse reference genome (mm10). Differential PSI = 0.04584. (**D**) Exon skipping is observed in *Rpgrip1* transcripts from bulk retinal RNA-seq. Reads were mapped to the mouse reference genome (mm10). Differential PSI = −0.244. (**E**) RT-PCR using retinal RNA from mutant and wildtype mice confirms that intron retention in *Cnga1* transcripts are specific to the mutant retina. (**F**) Immunofluorescent staining for Cnga1 in retinal cross sections of 2-month-old homozygous and heterozygous mutant mice shows a decrease in protein staining in the outer segments of homozygous mutant mice. Localization of Cnga1 to the outer segments of rod photoreceptors is correct in both mutant and control retinas. (**G**) Immunofluorescent staining for CHOP (red, arrows) indicates ER stress activation in 4-month-old mutant retina but not in control or at 2 months of age. Tissues were counterstained in DAPI (blue).

driving the disease as we have already observed evidence that ER stress is activated in the *Cwc27^K338fs/K338fs^* mouse retina, and we know from previous studies that this is one mechanism of photoreceptor degeneration. To confirm that the differential splicing is driving the photoreceptor degeneration through general stress pathways, further studies are needed to identify if any other downstream effects of the differential splicing can be observed, such as intron retention resulting in an innate immune response. The scRNA-sequencing suggests that the MG cells have upregulation of anti-viral associated genes, it would be interesting to see if the retinal pigmented epithelial cells also show this signature and if they have any significant degenerative or dysfunctional phenotypes in the *Cwc27^K338fs/K338fs^* mouse. Application of conditional knockouts would further allow us to determine if the severity of the *Cwc27* variant changes the molecular phenotype significantly and if future therapeutic interventions could be variant-dependent.

Materials and Methods
Animals
All animal procedures and experiments complied with a protocol approved by the Baylor College of Medicine IACUC.

Electroretinography
To quantify the extent and determine the progression of retinal dysfunction *in vivo*, ERG was performed on *Cwc27^K338fs/K338fs^* and *Cwc27^K338fs/+^* mice ($n \geq 3$) at multiple timepoints. Mice are dark adapted overnight before the start of ERG experiments. An intra-peritoneal injection of combo rodent-III (ketamine 22 mg/kg, xylazine 4.4 mg/kg and acepromazine 0.37 mg/kg) was used to anesthetize the mice. Tropicamide (1%), phenylephrine hydrochloride (2.5%), proparacaine hydrochloride (0.5%) and Goniosoft (2.5%) ophthalmic drops were administered to the mouse eyes. Mice were placed on a heated pad, an electrode (LKC Technologies, #95-033 M) was placed on each eye and a ground electrode was placed subcutaneously. Data acquisition and storage was managed with LKC UTAS Visual Diagnostic System and EMWIN software (LKC Technologies, Gaithersburg, MD, USA). Scotopic ERGs were conducted with flash intensities of 0.1, 1, 2.5 and 25 cd*s/m^2. Mice were light adapted to a white background light (30 cd*s/m^2) for 10 min and then photopic ERGs were conducted with flash intensities of 2.5, 25 and 790.5694 cd*s/m^2. Scotopic and photopic ERG results were analyzed and plotted using GraphPad Prism 8. Two-tailed unpaired *t*-test was performed for each stimulus intensity.

Hematoxylin and eosin staining
Hematoxylin and eosin (H&E) staining was performed in order to visualize the retinal cells and assess changes to the retina morphology. The eyes of *Cwc27^K338fs/K338fs^* and *Cwc27^K338fs/+^* mice ($n = 3$ per genotype) were enucleated

and fixed in fresh Davidson's fixative overnight at 4°C. The eyes were then incubated at 4°C in a series of ethanol dilutions (50, 70, 95 and 100% in PBS) for 1 h each followed by an overnight incubation in 100% ethanol. Eyes were then incubated in xylenes for 2 h at room temperature. After transferring to cassettes, eyes were incubated at 60°C in 50% xylenes/50% paraffin (w/v) for 2 h and then 100% paraffin overnight. After embedding the eyes in 100% paraffin, they were sectioned at 7 μm (Leica RM2255). Sections were deparaffinized in xylenes and rehydrated through the ethanol series (100, 95, 70 and 50% in water) and diH$_2$O for 5 min each. After rehydration, retinal cross-sections were stained with hematoxylin (Fisher Scientific, Hampton, New Hampshire #SH26-500D) and counterstained with eosin (EMS, #26051–21). Tissue sections were then mounted in Permount mounting medium (Fisher, #SP15–100), cover slipped and allowed to air dry overnight. The H&E-stained sections were imaged using light microscopy (Zeiss Axio Obsesrver.Z1) and the number of nuclei layers in the outer nuclear layer (ONL) was measured using ImageJ software and analyzed and plotted using GraphPad Prism 8. Two-tailed unpaired *t*-test was performed for each measurement.

Bulk RNA sequencing
Bulk RNA-sequencing was performed to evaluate the transcriptome for both gene expression and splicing pattern changes in the mutant retina. Total RNA was isolated from mutant ($n = 3$) and wildtype ($n = 6$) mouse retinas using the Direct-zol RNA Miniprep Kit (Zymo Research, #R2051) following the standard protocol for tissues and using pestle for tissue homogenization in microtubes. Next, the RNA-seq library was made using KAPA Stranded mRNA-Seq Library Preparation kit (Roche, Basel, Switzerland #KK8420). Briefly, the library was prepared by purifying poly-A RNA from total RNA using the Dynabeads mRNA Purification Kit (ThermoFisher, #61006), fragmenting the RNA to small size using heat and magnesium, and then 1st strand cDNA was synthesized using random primers. Next, 2nd strand cDNA was synthesized and marked with dUTP. The resultant cDNA was used for end repair, A-tailing and adaptor ligation steps. Finally, the library was amplified before sequencing on the Novaseq 6000 platform (Illumina). The strand marked with dUTP will not be amplified, allowing for strand-specific sequencing.

Bulk RNA sequencing data analysis
The bulk RNA-seq data were analyzed to identify any significant gene expression or splicing pattern changes in the mutant retina compared with the wildtype retina transcriptome. The paired-end bulk RNA-seq reads were aligned to a custom build mouse genome (GRCm38) index that includes all GRCm38 transcripts and SNPs with hisat2.2.1. Among the nine samples, six of them have an RNA-seq read length of 100 bp, and three of them have an RNA-seq read length of 151 bp. The

three samples with a read length of 151 bp were hard trimmed into reads with a length of 100 bp before downstream analysis. The read count per gene per sample was generated using HTSeq-count (version 0.13.5), based on Mus_musculus.GRCm38.101.chr.gtf downloaded from http://ftp.ensembl.org/pub/release-101/gtf/mus_musculus/. The number of total reads per sample ranges from 29 732 386 to 54 159 725, with a mean of 42 835 609 reads. The overall alignment rate ranges from 94 to 99%. DGE was performed with DESeq2 (version 1.30.0) (45) (for the genes with the total RNA-seq read counts from the nine samples per gene ≥10) using the adjusted *P*-value < 0.05 and $\log_2$ FC < −0.6 and >0.6 as cutoffs.

The intron retention analysis was performed with custom R script including the R libraries Rsubread (version 2.2.6) (46) and DEXSeq (version 1.34.1) (47). We first computed intron retention PSI based on the read counts mapping to the intron and the read counts mapping to the flanking exonic sequences of the intron (to avoid the 3′ RNA-sequencing bias) with Rsubread. Then, we compared the intron retention PSI of the same intron between Cwc27 mutant and wildtype sample groups with DEXSeq for all introns. Only the introns with mean FPKM of flanking exons ≥10 were considered. The significant intron retention events were determined with differential PSI between MT and WT ≥ 0.024 or ≤−0.029 (based on 2.5 and 97.5% quantile of differential PSI value distribution) and adjusted *P*-value ≤ 0.001 (the adjusted *P*-value is computed by DEXSeq). For the genotype samples with intron retention, we also required the intron retention PSI of each replicate sample of the corresponding genotype >0. The introns overlapped with any coding or noncoding exonic regions were filtered out.

The analysis of other splicing events was performed with rmats-turbo_4.1.0 (48) (with the parameters: *t* paired—readLength 100—variable-read-length—novelSS —libType fr-firststrand). We filtered the longer alternative exon with the length longer than the twice of the length of the shorter alternative exon to avoid analysis artifact. We required the average number of junction reads for at least one exon isoform in the samples associated with at least one genotype >10. The differential PSI cutoffs for each type of splicing events, including alternative 5′ splicing site, alternative 3′ splicing site and cassette exons, were taken based on the 2.5 and 97.5% percentile of the differential PSI value distribution and FDR ≤ 0.01 (the FDR is computed by rmats-turbo). For the genotype samples with upregulated PSI, we also required the PSI of each replicate sample of the corresponding genotype >0.

10× 3′ single cell RNA sequencing

To determine if there were any cell-type-specific gene expression changes, single cell RNA sequencing was performed on mutant (*n* = 1) and wildtype (*n* = 1) mouse retinas. The retinal cups were harvested from the mice and then were dissociated using a modified version of a previously described papain-based enzymatic digestion

protocol (49). Briefly, a solution of 45 U of activated papain (Worthington Biochemical, Lakewood, New Jersey #LS003126), 1 mg L-cysteine (Sigma, Darmstadt, Germany #C1276) and 8000 U of DNase I in 5 mL of PBS was added to the retinal cup and incubated for 15 min at 37°C to release live cells into a single-cell suspension. A solution of ovomucoid (15 mg; Worthington Biochemical, #NC9931428) and bovine serum albumin (15 mg; ThermoFisher Scientific, #B14) in 10 mL of PBS was added to deactivate the papain. Any remaining cell clumps were triturated in additional ovomucoid solution and filtered through 20 μm plastic mesh. This was repeated until the retina was in a single-cell suspension with no remaining cell clumps. Cells were resuspended in 2% FBS in PBS (ThermoFisher Scientific, #10439024) at a concentration of 1 M/mL and were then used for scRNA-seq. The single cell Gene Expression Library was prepared according to the Chromium Next GEM Single Cell 3′ GEM, Library and Gel Bead Kit (10x Genomics, Pleasanton, California #1000128). Briefly, single cells, reverse transcription (RT) reagents, gel beads containing barcoded oligonucleotides and oil were loaded on a Chromium controller (10x Genomics) to generate single cell GEMS (Gel Beads-In-Emulsions) where full length cDNA was synthesized and barcoded for each single cell. Subsequently, the GEMS are broken and cDNA from each single cell are pooled. Following cleanup using Dynabeads MyOne Silane Beads (ThermoFisher, #37002D), cDNA is amplified by PCR. The amplified product was fragmented to optimal size before end-repair, A-tailing, and adaptor ligation steps were performed. The final library was generated by amplification.

10× 3′ single cell RNA sequencing data analysis

The scRNA-seq data were analyzed to determine if there were any cell-type-specific gene expression changes observed in the mutant retina compared with wildtype. Two 10× Chip data per genotype sample were sequenced [two samples (retinas) from one mouse per genotype]. The 10× raw data were preprocessed with 10× Cell Ranger pipeline. A total of 12 606 and 11 117 cells were obtained from the mutant and wildtype samples, respectively. The mean reads per cell are about 36 698 and 33 428 for the mutant and wildtype samples, respectively. The gene by cell read count matrix per chip was filtered to remove low-quality cells with Seurat (version 3.9.9.9024) and doublets with DoubletFinder (version 2.0.3). Then, the four 10× Chip data (two 10× Chip data per sample) were integrated with the Seurat R package to generate the cell-type clusters per sample. The cell type of each cluster was assigned according to known gene markers of mouse retina cell types. After filtering out the low-quality cells, doublets and cells that cannot be assigned a cell type, single cell transcriptomes were obtained for 10 928 and 9473 individual cells from the mutant and wildtype retina, respectively. The median number of distinct transcripts detected per cell is 1263 for the mutant and 1005 for the wildtype samples.

The DGE analysis for each cell type between wildtype and mutant samples was performed using Wilcoxon rank sum test via the FindMarkers function of Seurat. The differentially expressed genes were identified with the adjusted P-value < 0.05 and $\log_2$ FC < −0.6 and >0.6 as cutoffs.

GO term enrichment analysis

To determine if there was any enrichment of up- or down-regulated genes in any biological pathways, we performed GO term enrichment analysis. The GO term enrichment analysis for the DEG from bulk RNA-seq and scRNA-seq and differential splicing genes from bulk RNA-seq was performed with enricher() function which applies hypergeometric test in clusterProfiler_3.16.1 R packages (50). Specifically, the functions msigdbr(), enricher(), emapplot() and dotplot() were applied with the default setting.

RT-PCR

To validate the intron retention observed by bulk and single cell RNA sequencing, RT-PCR was performed. The mouse retinas were dissected out and RNA was extracted following the Direct-zol RNA miniprep kit (Zymo Research, Irvine, California #R2051). The SuperScript III Reverse Transcription kit (Invitrogen, Waltham, Massachusetts #18080093) was used to generate cDNA. Two sets of primer pairs were designed which share the same forward primer (Cnga1-F: 5′-GCAGCACTTGCCAGGTACTAT-3′) in a flanking exon of the retained intron. The first reverse primer is in the other flanking exon of the retained intron (Cnga1-R1: 5′-TCCAGTTGTACATACACA-GGCAA-3′) and the second reverse primer is in the retained intron (Cnga1-R2: 5′-ggcattgatgcaacgtctgc-3′). The expected band size for F/R1 without IR is 308 and with IR is 394. The expected band size for F/R2 is 127.

Immunofluorescent staining

Immunofluorescent staining for markers was performed on retinal cross-sections to evaluate protein expression of affected transcripts and activation of stress pathways. Tissue sections were prepared, and paraffin-embedded retinal cross-sections were deparaffinized and rehydrated as previously described. Antigen retrieval was performed under heat in citrate buffer for CHOP staining and tris-EDTA for CNGA1 staining for 30 min. After slides were cooled and washed in PBS, tissue sections were incubated in 10% normal goat serum and 0.1% Tween-20 (NGST) in PBS for 1 h at room temperature in a humidified box. Primary antibodies anti-CNGA1 (1D1 PMC; a gift from Dr Robert Molday; 1:50) and anti-GADD153 (anti-CHOP; Santa Cruz, sc-575; 1:50) were diluted in NGST. Primary antibodies were applied to slides and allowed to incubate overnight at 4°C in a humidified chamber. The proceeding steps were performed in dim lighting or in a dark humidified chamber. Retinal sections were washed in PBS and then incubated in the appropriate secondary antibody

(Molecular Probes) diluted to 1:400 in NGST for 2 h at room temperature. After washing in PBS, retinal sections were counterstained with DAPI diluted at 1:1000 in PBS for 5 min at room temperature and then washed in PBS again. Sections were air dried for ∼5 min and then mounted with ProLong Gold mounting medium (Life Technologies, Carlsbad, California) and cover slipped. Stained sections were visualized using the Zeiss Axio Observer.Z1.

Supplementary Material

Supplementary Material is available at *HMG* online.

References

1. Di, C., Zayanti, S., Zhang, Q., Chen, Y., Wang, Y., Zhang, X., Liu, Y., Sun, C., Zhang, H. and Hoheisel, J.D. (2019) Function, clinical application, and strategies of pre-mRNA splicing in cancer. *Cell Death Differ.*, **26**, 1181–1194.
2. Ray, T.A., Cochran, K., Kozlowski, C., Wang, J., Alexander, G., Cady, M.A., Spencer, W.J., Ruzycki, P.A., Clark, B.S., Laeremans, A. *et al.* (2020) Comprehensive identification of mRNA isoforms reveals the diversity of neural cell-surface molecules with roles in retinal development and disease. *Nat. Commun.*, **11**, 3328.
3. Doorenweerd, N., Mahfouz, A., van Putten, M., Kaliyaperumal, R., PAC, T.H., Hendriksen, J.G.M., Aartsma-Rus, A.M., Verschuuren, J., Niks, E.H., Reinders, M.J.T. *et al.* (2017) Timing and localization of human dystrophin isoform expression provide insights into the cognitive phenotype of Duchenne muscular dystrophy. *Sci. Rep.*, **7**, 12575.
4. Hao, H., Veleri, S., Sun, B., Kim, D.S., Keeley, P.W., Kim, J.W., Yang, H.J., Yadav, S.P., Manjunath, S.H., Sood, R. *et al.* (2014) Regulation of a novel isoform of receptor expression enhancing protein REEP6 in rod photoreceptors by bZIP transcription factor NRL. *Hum. Mol. Genet.*, **23**, 4260–4271.
5. Saez, B., Walter, M.J. and Graubert, T.A. (2017) Splicing factor gene mutations in hematologic malignancies. *Blood*, **129**, 1260–1269.
6. Shiozawa, Y., Malcovati, L., Galli, A., Sato-Otsubo, A., Kataoka, K., Sato, Y., Watatani, Y., Suzuki, H., Yoshizato, T., Yoshida, K. *et al.* (2018) Aberrant splicing and defective mRNA production induced by somatic spliceosome mutations in myelodysplasia. *Nat. Commun.*, **9**, 3649.

7. Wood, K.A., Rowlands, C.F., Thomas, H.B., Woods, S., O'Flaherty, J., Douzgou, S., Kimber, S.J., Newman, W.G. and O'Keefe, R.T. (2020) Modelling the developmental spliceosomal craniofacial disorder Burn-McKeown syndrome using induced pluripotent stem cells. *PLoS One*, **15**, e0233582.

8. Favaro, F.P., Alvizi, L., Zechi-Ceide, R.M., Bertola, D., Felix, T.M., de Souza, J., Raskin, S., Twigg, S.R., Weiner, A.M., Armas, P. *et al.* (2014) A noncoding expansion in EIF4A3 causes Richieri-Costa-Pereira syndrome, a craniofacial disorder associated with limb defects. *Am. J. Hum. Genet.*, **94**, 120–128.

9. Beauchamp, M.C., Djedid, A., Bareke, E., Merkuri, F., Aber, R., Tam, A.S., Lines, M.A., Boycott, K.M., Stirling, P.C., Fish, J.L. *et al.* (2021) Mutation in Eftud2 causes craniofacial defects in mice via mis-splicing of Mdm2 and increased P53. *Hum. Mol. Genet.*, **30**, 739–757.

10. Buskin, A., Zhu, L., Chichagova, V., Basu, B., Mozaffari-Jovin, S., Dolan, D., Droop, A., Collin, J., Bronstein, R., Mehrotra, S. *et al.* (2018) Disrupted alternative splicing for genes implicated in splicing and ciliogenesis causes PRPF31 retinitis pigmentosa. *Nat. Commun.*, **9**, 4234.

11. Chen, X., Liu, Y., Sheng, X., Tam, P.O., Zhao, K., Chen, X., Rong, W., Liu, Y., Liu, X., Pan, X. *et al.* (2014) PRPF4 mutations cause autosomal dominant retinitis pigmentosa. *Hum. Mol. Genet.*, **23**, 2926–2939.

12. Jangi, M., Fleet, C., Cullen, P., Gupta, S.V., Mekhoubad, S., Chiao, E., Allaire, N., Bennett, C.F., Rigo, F., Krainer, A.R. *et al.* (2017) SMN deficiency in severe models of spinal muscular atrophy causes widespread intron retention and DNA damage. *Proc. Natl. Acad. Sci. U. S. A.*, **114**, E2347–E2356.

13. Tanackovic, G., Ransijn, A., Ayuso, C., Harper, S., Berson, E.L. and Rivolta, C. (2011) A missense mutation in PRPF6 causes impairment of pre-mRNA splicing and autosomal-dominant retinitis pigmentosa. *Am. J. Hum. Genet.*, **88**, 643–649.

14. Towns, K.V., Kipioti, A., Long, V., McKibbin, M., Maubaret, C., Vaclavik, V., Ehsani, P., Springell, K., Kamal, M., Ramesar, R.S. *et al.* (2010) Prognosis for splicing factor PRPF8 retinitis pigmentosa, novel mutations and correlation between human and yeast phenotypes. *Hum. Mutat.*, **31**, E1361–E1376.

15. Azizzadeh Pormehr, L., Ahmadian, S., Daftarian, N., Mousavi, S.A. and Shafiezadeh, M. (2020) PRPF31 reduction causes mis-splicing of the phototransduction genes in human organotypic retinal culture. *Eur. J. Hum. Genet.*, **28**, 491–498.

16. Doktor, T.K., Hua, Y., Andersen, H.S., Broner, S., Liu, Y.H., Wieckowska, A., Dembic, M., Bruun, G.H., Krainer, A.R. and Andresen, B.S. (2017) RNA-sequencing of a mouse-model of spinal muscular atrophy reveals tissue-wide changes in splicing of U12-dependent introns. *Nucleic Acids Res.*, **45**, 395–416.

17. Xiao, X., Cao, Y., Zhang, Z., Xu, Y., Zheng, Y., Chen, L.J., Pang, C.P. and Chen, H. (2017) Novel mutations in PRPF31 causing retinitis pigmentosa identified using whole-exome sequencing. *IOVS.*, **58**, 6342–6350.

18. Yusuf, I.H., Birtel, J., Shanks, M.E., Clouston, P., Downes, S.M., Charbel Issa, P. and Mac Laren, R.E. (2019) Clinical characterization of retinitis pigmentosa associated with variants in SNRNP200. *JAMA Ophthalmol.*, **137**, 1295–1300.

19. Farkas, M.H., Lew, D.S., Sousa, M.E., Bujakowska, K., Chatagnon, J., Bhattacharya, S.S., Pierce, E.A. and Nandrot, E.F. (2014) Mutations in pre-mRNA processing factors 3, 8, and 31 cause dysfunction of the retinal pigment epithelium. *Am. J. Pathol.*, **184**, 2641–2652.

20. Graziotto, J.J., Farkas, M.H., Bujakowska, K., Deramaudt, B.M., Zhang, Q., Nandrot, E.F., Inglehearn, C.F., Bhattacharya, S.S. and Pierce, E.A. (2011) Three gene-targeted mouse models of RNA splicing factor RP show late-onset RPE and retinal degeneration. *Invest. Ophthalmol. Vis. Sci.*, **52**, 190–198.

21. Valdes-Sanchez, L., Calado, S.M., de la Cerda, B., Aramburu, A., Garcia-Delgado, A.B., Massalini, S., Montero-Sanchez, A., Bhatia, V., Rodriguez-Bocanegra, E., Diez-Lloret, A. *et al.* (2019) Retinal pigment epithelium degeneration caused by aggregation of PRPF31 and the role of HSP70 family of proteins. *Mol. Med.*, **26**, 1.

22. Li, J., Liu, F., Lv, Y., Sun, K., Zhao, Y., Reilly, J., Zhang, Y., Tu, J., Yu, S., Liu, X. *et al.* (2021) Prpf31 is essential for the survival and differentiation of retinal progenitor cells by modulating alternative splicing. *Nucleic Acids Res.*, **49**, 2027–2043.

23. Keightley, M.C., Crowhurst, M.O., Layton, J.E., Beilharz, T., Markmiller, S., Varma, S., Hogan, B.M., de Jong-Curtain, T.A., Heath, J.K. and Lieschke, G.J. (2013) In vivo mutation of pre-mRNA processing factor 8 (Prpf8) affects transcript splicing, cell survival and myeloid differentiation. *FEBS Lett.*, **587**, 2150–2157.

24. Wickramasinghe, V.O., Gonzalez-Porta, M., Perera, D., Bartolozzi, A.R., Sibley, C.R., Hallegger, M., Ule, J., Marioni, J.C. and Venkitaraman, A.R. (2015) Regulation of constitutive and alternative mRNA splicing across the human transcriptome by PRPF8 is determined by 5′ splice site strength. *Genome Biol.*, **16**, 201.

25. Brea-Fernandez, A.J., Cabanas, P., Dacruz-Alvarez, D., Caamano, P., Limeres, J. and Loidi, L. (2019) Expanding the clinical and molecular spectrum of the CWC27-related spliceosomopathy. *J. Hum. Genet.*, **64**, 1133–1136.

26. Xu, M., Xie, Y.A., Abouzeid, H., Gordon, C.T., Fiorentino, A., Sun, Z., Lehman, A., Osman, I.S., Dharmat, R., Riveiro-Alvarez, R. *et al.* (2017) Mutations in the spliceosome component CWC27 cause retinal degeneration with or without additional developmental anomalies. *Am. J. Hum. Genet.*, **100**, 592–604.

27. Ulrich, A. and Wahl, M.C. (2014) Structure and evolution of the spliceosomal peptidyl-prolyl cis-trans isomerase Cwc27. *Acta Crystallogr. D Biol. Crystallogr.*, **70**, 3110–3123.

28. Busetto, V., Barbosa, I., Basquin, J., Marquenet, E., Hocq, R., Hennion, M., Paternina, J.A., Namane, A., Conti, E., Bensaude, O. *et al.* (2020) Structural and functional insights into CWC27/CWC22 heterodimer linking the exon junction complex to spliceosomes. *Nucleic Acids Res.*, **48**, 5670–5683.

29. Davis, T.L., Walker, J.R., Campagna-Slater, V., Finerty, P.J., Paramanathan, R., Bernstein, G., Mac Kenzie, F., Tempel, W., Ouyang, H., Lee, W.H. *et al.* (2010) Structural and biochemical characterization of the human cyclophilin family of peptidyl-prolyl isomerases. *PLoS Biol.*, **8**, e1000439.

30. Alexandrov, A., Colognori, D., Shu, M.D. and Steitz, J.A. (2012) Human spliceosomal protein CWC22 plays a role in coupling splicing to exon junction complex deposition and nonsense-mediated decay. *Proc. Natl. Acad. Sci. U. S. A.*, **109**, 21313–21318.

31. Zhang, X., Yan, C., Zhan, X., Li, L., Lei, J. and Shi, Y. (2018) Structure of the human activated spliceosome in three conformational states. *Cell Res.*, **28**, 307–322.

32. Winzeler, E.A., Shoemaker, D.D., Astromoff, A., Liang, H., Anderson, K., Andre, B., Bangham, R., Benito, R., Boeke, J.D., Bussey, H. *et al.* (1999) Functional characterization of the S. cerevisiae genome by gene deletion and parallel analysis. *Sci.*, **285**, 901–906.

33. Giaever, G., Chu, A.M., Ni, L., Connelly, C., Riles, L., Ve'ronneau, S., Dow, S., Lucau-Danila, A., Anderson, K., Andre´, B. *et al.* (2002) Functional profiling of the Saccharomyces cerevisiae genome. *Nature*, **418**, 1244–1256.

34. Ohrt, T., Prior, M., Dannenberg, J., Odenwalder, P., Dybkov, O., Rasche, N., Schmitzova, J., Gregor, I., Fabrizio, P., Enderlein, J. *et al.* (2012) Prp2-mediated protein rearrangements at the catalytic core of the spliceosome as revealed by dcFCCS. *RNA*, **18**, 1244–1256.

35. Liberzon, A., Birger, C., Thorvaldsdottir, H., Ghandi, M., Mesirov, J.P. and Tamayo, P. (2015) The molecular signatures database (MSigDB) hallmark gene set collection. *Cell Syst.*, **1**, 417–425.

36. Liberzon, A., Subramanian, A., Pinchback, R., Thorvaldsdottir, H., Tamayo, P. and Mesirov, J.P. (2011) Molecular signatures database (MSigDB) 3.0. *Bioinformatics*, **27**, 1739–1740.

37. Subramanian, A., Tamayo, P., Mootha, V.K., Mukherjee, S., Ebert, B.L., Gillette, M.A., Paulovich, A., Pomeroy, S.L., Golub, T.R., Lander, E.S. *et al.* (2005) Gene set enrichment analysis: a knowledge-based approach for interpreting genome-wide expression profiles. *PNAS*, **102**, 15545–15550.

38. Hippert, C., Graca, A.B., Barber, A.C., West, E.L., Smith, A.J., Ali, R.R. and Pearson, R.A. (2015) Muller glia activation in response to inherited retinal degeneration is highly varied and disease-specific. *PLoS One*, **10**, e0120415.

39. Liu, Y., Wang, C. and Su, G. (2019) Cellular signaling in Muller glia: progenitor cells for regenerative and neuroprotective responses in pharmacological models of retinal degeneration. *J. Ophthalmol.*, **2019**, 5743109.

40. Yu, G., Wang, L.G., Yan, G.R. and He, Q.Y. (2015) DOSE: an R/Bioconductor package for disease ontology semantic and enrichment analysis. *Bioinformatics*, **31**, 608–609.

41. Katagiri, S., Akahori, M., Sergeev, Y., Yoshitake, K., Ikeo, K., Furuno, M., Hayashi, T., Kondo, M., Ueno, S., Tsunoda, K. *et al.* (2014) Whole exome analysis identifies frequent CNGA1 mutations in Japanese population with autosomal recessive retinitis pigmentosa. *PLoS One*, **9**, e108721.

42. Bowling, E.A., Wang, J.H., Gong, F., Wu, W., Neill, N.J., Kim, I.S., Tyagi, S., Orellana, M., Kurley, S.J., Dominguez-Vidana, R. *et al.* (2021) Spliceosome-targeted therapies trigger an antiviral immune response in triple-negative breast cancer. *Cell*, **184**, 384, e321–403.

43. Eskens, F.A., Ramos, F.J., Burger, H., O'Brien, J.P., Piera, A., de Jonge, M.J., Mizui, Y., Wiemer, E.A., Carreras, M.J., Baselga, J. *et al.* (2013) Phase I pharmacokinetic and pharmacodynamic study of the first-in-class spliceosome inhibitor E7107 in patients with advanced solid tumors. *Clin. Cancer Res.*, **19**, 6296–6304.

44. Hong, D.S., Kurzrock, R., Naing, A., Wheler, J.J., Falchook, G.S., Schiffman, J.S., Faulkner, N., Pilat, M.J., O'Brien, J. and LoRusso, P. (2014) A phase I, open-label, single-arm, dose-escalation study of E7107, a precursor messenger ribonucleic acid (pre-mRNA) spliceosome inhibitor administered intravenously on days 1 and 8 every 21 days to patients with solid tumors. *Investig. New Drugs*, **32**, 436–444.

45. Love, M.I., Huber, W. and Anders, S. (2014) Moderated estimation of fold change and dispersion for RNA-seq data with DESeq2. *Genome Biol.*, **15**, 550.

46. Liao, Y., Smyth, G.K. and Shi, W. (2019) The R package Rsubread is easier, faster, cheaper and better for alignment and quantification of RNA sequencing reads. *Nucleic Acids Res.*, **47**, e47.

47. Anders, S., Reyes, A. and Huber, W. (2012) Detecting differential usage of exons from RNA-Seq data. *Genome Res.*, **22**, 2008–2017.

48. Shen, S., Park, J.W., Lu, Z.X., Lin, L., Henry, M.D., Wu, Y.N., Zhou, Q. and Xing, Y. (2014) rMATS: robust and flexible detection of differential alternative splicing from replicate RNA-Seq data. *Proc. Natl. Acad. Sci. U. S. A.*, **111**, E5593–E5601.

49. Siegert, S., Cabuy, E., Scherf, B.G., Kohler, H., Panda, S., Le, Y.Z., Fehling, H.J., Gaidatzis, D., Stadler, M.B. and Roska, B. (2012) Transcriptional code and disease map for adult retinal cell types. *Nat. Neurosci.*, **15**, 487, S481-482–495.

50. Yu, G., Wang, L.G., Han, Y. and He, Q.Y. (2012) Cluster profiler: an R package for comparing biological themes among gene clusters. *OMICS*, **16**, 284–287.